Dynamical aspects of ^{48}Ti + ^{58}Fe, ^{58}Ni → ^{106}Cd*, ^{106}Sn* reactions at energies near the Coulomb barrier

Rupinder Kaur,[1,2,3,*] Maninder Kaur,[2] Varinderjit Singh,[2] Mandeep Kaur,[3] BirBikram Singh,[3,†] and B. S. Sandhu[1]

[1]*Department of Physics, Punjabi University, Patiala-147002, India*

[2]*Department of Physical Sciences, I.K.G. Punjab Technical University, Kapurthala-144603, India*

[3]*Department of Physics, Sri Guru Granth Sahib World University, Fatehgarh Sahib-140406, India*

(Received 12 June 2019; revised manuscript received 10 January 2020; accepted 9 March 2020; published 14 April 2020)

The study of the heavy-ion reactions at the near- and sub-barrier regimes gives immense information about the nuclear structure and the involved reaction dynamics. It has been observed that a slight difference in the nuclear structure may lead to a significant change in the sub-barrier fusion excitation functions. The studies of different trends of excitation functions below the Coulomb barrier region due to dissimilar structures of the nuclei, which are involved in the reaction, are available in literature. To understand the role of different structures and dynamics involved in such reactions, an investigation of ^{48}Ti-induced reactions on ^{58}Fe and ^{58}Ni forming ^{106}Cd* and ^{106}Sn* compound nuclei (CN), respectively, has been made at similar $E_{\mathrm{c.m.}}/V_b$ values within the framework of the dynamical cluster decay model (DCM). The difference in the structure between the nuclei is quite notable with ^{58}Ni and ^{106}Sn* having a proton shell closure ($Z = 28$ and 50, respectively). Within the DCM, the experimental fusion evaporation cross sections are reproduced using deformed configurations effects included up to quadruple deformations (β_{2i}) for two nuclei having optimum orientations $\theta^{\mathrm{opt.}}$. The fusion evaporation data at near- and sub-barriers has been explained through the calculated enhanced ΣP_0 values of the decaying channels in the case of ^{106}Cd* in comparison to ^{106}Sn*. Moreover, it is observed that the quantum tunneling of the fragments is less hindered in the case of ^{106}Cd* as compared to ^{106}Sn* at the lower values of $E_{\mathrm{c.m.}}/V_b$, i.e., having less barrier modification (ΔV_B) in the case of the former. The role of magicity has been further explored with the plotted values of the ratio of fusion cross sections (σ_{fus}) of CN ^{106}Sn* and ^{112}Xe* (formed in the reaction with both the projectile ^{58}Ni and target ^{54}Fe having proton and neutron magicity, respectively) with respect to ^{106}Cd*, which are highly suppressed in the case of the latter in comparison to the former, particularly, below the Coulomb barrier.

DOI: 10.1103/PhysRevC.101.044605

I. INTRODUCTION

In the past few decades, a thorough study of sub-barrier heavy-ion interactions have uncovered the various unexpected characteristics involved in the reaction dynamics. The most notable outcome of these studies, observed experimentally, is the hinderance phenomenon at deep sub-barrier energies in some systems in comparison to others. This suggests existence of an experimentally determined threshold limit E_s in sub-barrier energies which varies from one system to another. The investigation of the physical cause for such phenomena will help to understand the involved reaction dynamics. Thus, to ascertain the reaction mechanisms involved in observed phenomena requires a consistent study of various systems. The apparent dynamical picture of the sub-barrier fusion has been acknowledged by the considerable experimental and theoretical efforts made by various authors in this direction [1]. Several experiments have provided a clear example of fusion hindrance at the deep sub-barrier region. One of such studies in which the effect on the fusion excitation function due to the associated nuclear structure of the interacting nuclei, has been investigated by Jiang *et al.* in ^{64}Ni + ^{64}Ni fusion reaction [2]. The author has explained the associated phenomenon of hinderance by considering stiff to open-shell nuclei in the entrance channel in the sub-barrier regime in terms of the S factor where the steep falloff in cross sections translates into a maximum of the S factor. Fusion hindrance in the ^{58}Ni + ^{54}Fe reaction at lower energies is also investigated by Stefanini *et al.* [3]. They observed that, at lower energies, fusion cross sections drop faster than conventional Woods-Saxon potential calculations with a steep slope. Recently, Stefanini *et al.* [4] have also shown that distinct low-energy nuclear structures of the involved nuclei leads to different trends in the fusion excitations functions for the ^{48}Ti + ^{58}Fe and ^{58}Ni + ^{54}Fe reactions at the sub-barrier regime. Large fusion cross sections has been observed in the measured energy range in ^{48}Ti + ^{58}Fe as compared to ^{58}Ni + ^{54}Fe (with closed-shell protons and neutrons in the entrance channel). The cross-section trends are explained in the ^{48}Ti + ^{58}Fe reaction through the involved strong quadrupole modes of both ^{48}Ti and ^{58}Fe and the two-neutron transfer channel.

*roopisaini87@gmail.com

†birbikramsingh@sggswu.edu.in

Theoretically, the observed hindrance phenomenon in heavy-ion fusion reactions has been explained through an ion-ion potential which produces a shallow pocket arising from nuclear incompressibility [5]. Dasso and Pollarolo have also found that a shallow potential is needed to describe the experimental data for the fusion of the ^{60}Ni and ^{89}Y reaction [6]. Ichikawa *et al.* proposed an adiabatic approach by adding damping factor to the coupling matrix elements at very low energy in the coupled channel model which reproduces data at below barrier energies [7]. Various other examples of fusion hindrance in the sub-barrier regime and the possible structural and dynamical effects involved are available in the literature [8]. These studies have established that the nuclear structure of the colliding nuclei can determine the nature of the interaction, or, conversely, the data obtained in the sub-barrier fusion helps in extracting the information about the possible nuclear structure.

In view of above observations of fusion hinderance, it will be interesting to investigate the dynamical aspects associated with reactions involving different nuclear structural effects within the clusterization approach of the dynamical cluster decay model (DCM) [9–26]. In the present paper, we have performed calculations to explore the dynamical aspects related to the ^{48}Ti-induced reactions on ^{58}Fe and ^{58}Ni targets forming compound nuclei ^{106}Cd* and ^{106}Sn*, respectively, at similar $E_{\rm c.m.}/V_b$ values [4]. In one of the fusion reactions, the target ^{58}Ni has proton shell closure, $Z = 28$ and the compound nucleus ^{106}Sn* populated through this reaction also have proton shell closures, i.e., $Z = 50$. We will try to investigate the influence of involved stiff nuclei and open-shell nuclei on the fusion cross section. The cross sections are obtained for β_2-deformed nuclei having optimum orientations through the empirically fitted neck length parameter (ΔR) values. Generally, the dynamics of neck region are quite different when the two nuclei approach each other in contrast to when they rebound. The neck shrinks rather slowly as the nuclei separate [28]. In the present paper, the neck effects are observed for the decaying fragments within the framework of the DCM, particularly, for light particles (LPs) ($1 < A \leqslant 4$) or evaporation residue (ER) using hydrodynamical mass parameters of Kröger and Scheid based on the hydrodynamical flow [29]. The indispensable role of the structure of the decaying fragments has also been explored through the preformation probabilities obtained from the calculated fragmentation potentials. The barrier-lowering parameter and the summed up preformation of fragments have been used to address the observed hindrance at sub-barrier energies.

The paper has been organized as follows: Sec. II gives a brief account of the dynamical cluster-decay model. The calculations and results for excitation functions of both CNs are discussed in Sec. III. Finally, the results are summarized in Sec. IV.

II. THE DYNAMICAL CLUSTER-DECAY MODEL FOR THE HOT AND ROTATING COMPOUND SYSTEM

The dynamical cluster-decay model is based on the quantum-mechanical fragmentation theory [30]. This model has been successfully used to carry out the theoretical calculations in light, medium, and heavy mass regions [9–26]. In the model, all possible decay modes of a compound nucleus via emission of LPs, $A \leqslant 4$ (results in evaporation residues), intermediate mass fragments, $5 \leqslant A \leqslant 20$, and fission fragments (FFs), $A/2 \pm 20$ can be dealt with. The model can also be used to study noncompound nucleus (nCN) reactions, such as quasifission, deep in elastic orbiting, etc. In contrast to the statistical models, it treats all the fragmentation processes on equal footing as the dynamical collective mass motion with different quantum-mechanical probabilities through the barrier. Thus, it can describe the much needed dynamical picture involved in the decay process.

In the model, the calculations are carried out in terms of two coordinates. The first coordinate is the collective coordinates of mass asymmetry (and charge asymmetry) $\eta_A = (A_1 - A_2)/(A_1 + A_2)$ [and $\eta_Z = (Z_1 - Z_2)/(Z_1 + Z_2)$] where the subscripts 1 and 2 stand for heavy and light fragments, respectively, and the second is the relative separation coordinate R between two nuclei or, in general, between two fragments with deformation effects from quadruple to hexadecupole $\beta_{\lambda i}$ ($\lambda = 2$–4, $i = 1, 2$), and optimum orientation $\theta_i^{\rm opt.}$. Here, the first coordinate η refers to the nucleon division (or exchange) between outgoing fragments. The separation coordinate R, characterizes the transfer of kinetic energy of the incoming channel ($E_{\rm c.m.}$) to internal excitation [total excitation energy or total kinetic energy (TKE)] of the outgoing channel. The CN decay cross section or the fragment production cross section can be defined in terms of these coordinates for different ℓ-partial waves and is given below,

$$\sigma = \sum_{\ell=0}^{\ell_{\rm max}} \sigma_\ell = \frac{\pi}{k^2} \sum_{\ell=0}^{\ell_{\rm max}} (2\ell + 1) P_0 P T_\ell, \qquad k = \sqrt{\frac{2\mu E_{\rm c.m.}}{\hbar^2}}, \tag{1}$$

where T_ℓ is the entrance channel penetration probability, i.e., the CN formation probability $T_\ell = 1$ for $\ell \leqslant \ell_{\rm max}$ and zero for $\ell > \ell_{\rm max}$. The term P_0 is called preformation probability and refers to η motion. It provides the significant information related to nuclear structure, and the term P known as penetrability refers to the R motion. Generally, the $\sigma_{\rm Fusion} = \sigma_{\rm ER} + \sigma_{\rm FF} + \sigma_{\rm nCN}$, where $\sigma_{\rm ER}$, $\sigma_{\rm FF}$, and $\sigma_{\rm nCN}$ are contributions towards total fusion cross section from evaporation residues, fusion-fission, and noncompound nucleus processes. But for the chosen systems under investigation at the near- and below-barrier regions, the fusion cross sections are observed to have contributions from ER alone, no nCN contribution is observed. Now, $\sigma_{\rm CN} = \sigma_{\rm ER} + \sigma_{\rm FF}$, and $\sigma_{\rm nCN}$ is calculated as

$$\sigma_{\rm nCN} = \sigma_{\rm Expt.Fus} - \sigma_{\rm Cal.Fus}. \tag{2}$$

Furthermore, in the statistical model language, the compound nucleus formation probability $P_{\rm CN}$ is also defined in terms of the compound nucleus-decay cross-section $\sigma_{\rm CN}$ as

$$P_{\rm CN} = \sigma_{\rm CN}/\sigma_{\rm Fusion} = 1 - \sigma_{\rm nCN}/\sigma_{\rm Fusion}, \tag{3}$$

which, for zero contribution of the nCN process, gives $P_{\rm CN}$ or $T_\ell = 1$. In other words, if $\sigma_{\rm nCN} = 0$, $P_{\rm CN} = 1$ then the reaction is a pure CN reaction. Thus, the determination of $P_{\rm CN}$ provides a possibility to understand the role of the $\sigma_{\rm nCN} = 0$ component in $\sigma_{\rm Fusion}$.

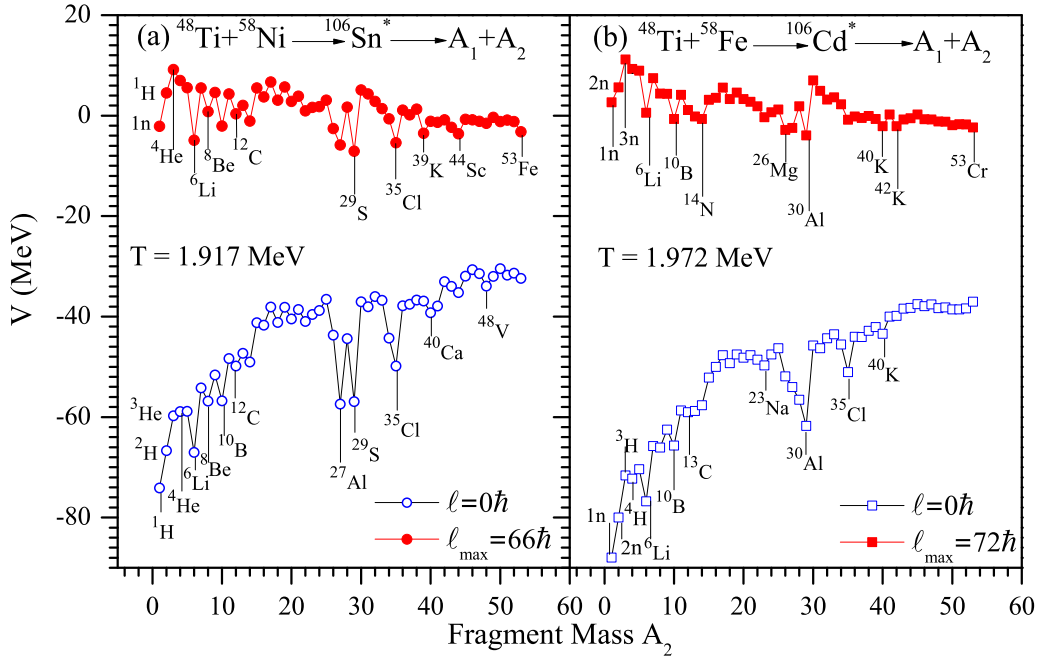

FIG. 1. The fragmentation potential V (MeV) as a function of fragment mass number A_2, calculated for two extreme ℓ values, for the CNs ^{106}Sn* and ^{106}Cd* at $E_{\rm c.m.}/V_b = 0.92$ and $\Delta R = 0.96$ fm for deformed fragmentation paths.

μ in Eq. (1) is referred to as the reduced mass ($\mu = \frac{A_1A_2}{A_1+A_2}m$), where m is the nucleon mass. $\ell_{\rm max}$ is known as the maximum angular momentum; it corresponds to the value of angular momentum ℓ for which $\sigma_{\rm ERs}$ becomes negligibly small.

The preformation probability $P_0(A_i) = |\psi_R[\eta(A_i)]|^2\sqrt{B_{\eta\eta}}\frac{2}{A^*_{\rm CN}}$ of fragments inside the CN is given by the solution of the stationary Schrödinger wave equation in η at fixed $R = R_a$,

$$\left\{-\frac{\hbar^2}{2\sqrt{B_{\eta\eta}}}\frac{\partial}{\partial\eta}\frac{1}{\sqrt{B_{\eta\eta}}}\frac{\partial}{\partial\eta} + V(R,\eta,T)\right\}\psi^{\nu}(\eta) = E^{\nu}\psi^{\nu}(\eta), \tag{4}$$

with $\nu = 0\text{–}3\cdots$ referring to ground-state ($\nu = 0$) and excited-state ($\nu = 1\text{–}3\cdots$) solutions and $i = 1$ or 2, for the heavy and light fragments, respectively, and assuming the Boltzmann-like occupation of excited states,

$$|\psi(\eta)|^2 = \sum_{\nu=0}^{\infty}|\psi^{\nu}(\eta)|^2\exp(-E^{\nu}/T). \tag{5}$$

In Eq. (4), the mass parameters $B_{\eta\eta}$ are the classical hydrodynamical masses [29].

The term R_a, which is defined as

$$R_a = R_1(\alpha_1,T) + R_2(\alpha_2,T) + \Delta R(T), \tag{6}$$

in the decay of the spherical as well as deformed and oriented reaction products, is the first turning point of the penetration path. For deformed and oriented nuclei, the formalism is generalized by using the radii R_1 and R_2 and is given by

$$R_i(\alpha_i,T) = R_{0i}(T)\left[1 + \sum_{\lambda}\beta_{\lambda i}Y^{(0)}_{\lambda}(\alpha_i)\right]. \tag{7}$$

α_i is the angle between the symmetry axis and the radius vector of the interacting nucleus and is measured in the clockwise direction with respect to the symmetry axis. The temperature-dependent nuclear radii $R_{0i}(T)$ for equivalent spherical nuclei are defined as $R_{0i}(T) = [1.28A_i^{1/3} - 0.76 + 0.8A_i^{-1/3}](1 + 0.0007T^2)$ [31], and T (in MeV) is related to $E^*_{\rm CN} = \frac{1}{9}AT^2 - T = E_{\rm c.m.} + Q_{\rm in}$ where $Q_{\rm in}$ is the Q value of the incoming channel. In Eq. (6), ΔR is the temperature-dependent neck-length parameter that assimilates the neck formation effects between two nuclei, whose value remains within the range of validity (∼2 fm) of the proximity potential, used here, and varies smoothly with the temperature of the CN.

The preformation probability P_0, which is an important component of the model, contains the structure information of the CN, and it enters via the minimized fragmentation potential. The fragmentation potential $[V_R(\eta,\ell,T)]$ profile is shown in Figs. 1 and 2 for differently chosen CNs, i.e., ^{106}Sn* [Figs. 1(a) and 2(a)], ^{106}Cd* [Figs. 1(b) and 2(b)], and is defined as the

$$\begin{aligned}V(R,\eta,\ell,T) &= \sum_{i=1}^{2}[V_{\rm LDM}(A_i,Z_i,T)] + \sum_{i=1}^{2}[\delta U_i]\exp\left(-T^2/T_0^2\right)\\ &+V_C(R,Z_i,\beta_{\lambda i},\theta_i,T) + V_P(R,A_i,\beta_{\lambda i},\theta_i,T)\\ &+V_{\ell}(R,A_i,\beta_{\lambda i},\theta_i,T).\end{aligned} \tag{8}$$

In the fragmentation potential equation mentioned above, $V_{\rm LDM}$ is the T-dependent liquid drop model energy from Davidson *et al.* [32], and $\delta U(T)$'s are the empirical shell correction from Myers and Swiatecki [33], which is also made T dependent to vanish exponentially with $T_0 = 1.5$ MeV [34].

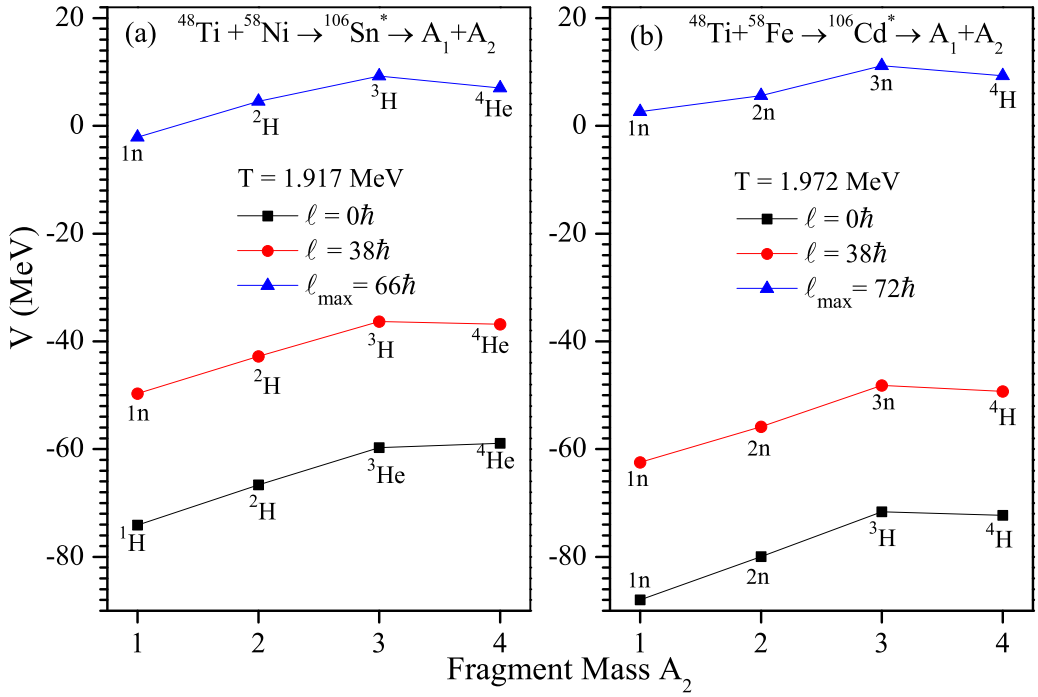

FIG. 2. The same as in Fig. 1 but for LPs, i.e., $A \leqslant 4$.

V_C, V_P, and V_ℓ, respectively, are known as the T-dependent Coulomb potential, the nuclear proximity potential [35], and the centrifugal part of the interaction process. The Coulomb potential for the two interacting hot, deformed, and oriented nuclei is given by

$$V_C(R, Z_i, \beta_{\lambda i}, \theta_i, T) = Z_1 Z_2 e^2/R(T) + 3Z_1 Z_2 e^2 \times \sum \frac{R_i^\lambda(\alpha_i, T)}{(2\lambda+1)} Y_\lambda^{(0_i)} \left[\beta_{\lambda i} + \frac{4}{7}\beta_{\lambda i}^2 Y_\lambda^{(0)}(\theta_i)\right]. \quad (9)$$

The deformation parameters ($\beta_{\lambda i}$) of the nuclei are taken from the tables of Moller *et al.* [36]. $Y_\lambda^{(0)}(\theta_i)$ are the spherical harmonic functions, and the orientation angle (θ_i) is the angle between the nuclear symmetry axis and the collision Z axis and is measured in the counterclockwise direction.

The term V_ℓ gives the centrifugal effects and is calculated by the equation,

$$V_\ell(R, A_i, \beta_{\lambda i}, \theta_i, T) = \hbar^2 \ell(\ell+1)/2I_s(T). \quad (10)$$

In the above expression, $I_s(T)$ is the moment of inertia and used in the sticking limit, which is more appropriate for proximity potential (nuclear surface $\leqslant 2$ fm), i.e.,

$$I = I_s(T) = \mu R^2 + \frac{2}{5}A_1 m R_1^2(\alpha_1, T) + \frac{2}{5}A_2 m R_2^2(\alpha_2, T). \quad (11)$$

Now, the term P known as the penetration probability (or the tunneling probability) used in calculating the cross section as given in Eq. (1), is calculated as the Wentzel-Kramers-Brillouin tunneling probability,

$$P = \exp\left[\frac{-2}{\hbar}\int_{R_a}^{R_b}\sqrt{2\mu[V(R) - V(R_a)]}dR\right] \quad (12)$$

solved analytically [37]. R_a and R_b mentioned in Eq. (12) and shown in Figs. 3(a) and 3(b) are the first and second turning points, satisfying

$$V(R_a) = V(R_b) = Q_{\rm eff} = {\rm TKE}(T). \quad (13)$$

Just like $Q_{\rm out}$ in the case of spontaneous ($T = 0$) cluster decay [9], the potential $V(R_a)$ can be looked upon as the effective positive Q value $Q_{\rm eff}(T, \ell)[= {\rm TKE}(T)]$ for the decay of the hot compound nucleus. Using Eq. (11), $R_b(\ell)$ is given by ℓ-dependent scattering potential at fixed T,

$$V(R, T, \ell) = [Z_H Z_L e^2/R(T)] + V_P(T) + V_\ell(T), \quad (14)$$

which is normalized to the exit channel binding energy. The choice of R_a [equivalently, ΔR in Eq. (4)] allows us to define, equivalently, the barrier-lowering parameter ΔV_B [38], which simply relates $V(R_a, \ell)$, and the top of the barrier $V_B(\ell)$ for each ℓ,

$$\Delta V_B = V(R_a, \ell) - V_B(\ell). \quad (15)$$

Here, $V(R_a, \ell)$ and $V_B(\ell)$ represent the actual barrier used for the penetration and the top barrier position, respectively. Note that ΔV_B is a negative quantity as the value of $V(R_a, \ell)$ being always smaller than $V_B(\ell)$. This implies that the barrier actually used to reproduce the cross sections is effectively lowered and this process of barrier lowering is depicted in Fig. 4(a), which presents the variation of ΔV_B (at $\ell_{\rm max}$) calculated for the CNs ^{106}Sn* and ^{106}Cd* as a function of $E_{\rm c.m.}/V_b$. This quantity of barrier lowering addresses the data at below the

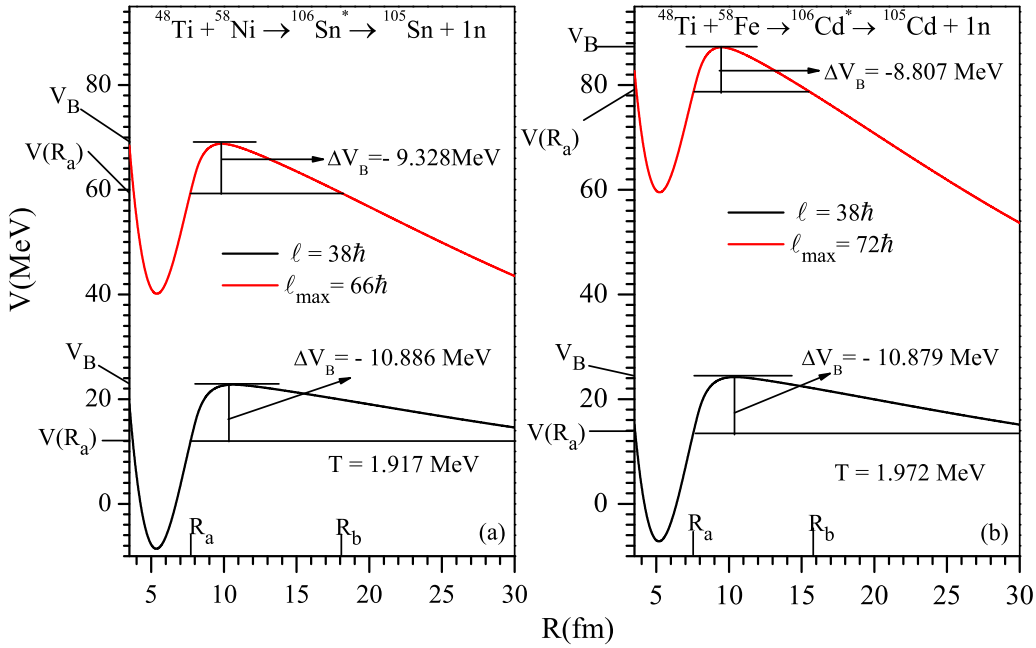

FIG. 3. The scattering potential $V(R, \ell)$ as a function of R (fm) for ^{106}Sn* and ^{106}Cd* at $E_{\text{c.m.}}/V_b = 0.92$ at the two ℓ values. The barrier-lowering parameter ΔV_B is also mentioned at lower ℓ and $\ell_{\max}$ values.

barrier region to explain the observed hindrance phenomenon, discussed in the next section.

III. CALCULATIONS AND DISCUSSIONS

The analysis of heavy-ion-induced fusion reactions across the Coulomb barrier has been performed within the DCM for ^{48}Ti + ^{58}Fe and ^{48}Ti + ^{58}Ni reactions populating CNs ^{106}Cd* and ^{106}Sn*, respectively. The calculations are performed by including deformation effects up to quadrupole deformation and with optimum orientations $\theta_i^{\text{opt.}}$. The experimental fusion cross sections (σ_{fus}) for compound nucleus ^{106}Cd* have been reproduced by using the neck-length parameter (ΔR) as a free parameter at various $E_{\text{c.m.}}/V_b$ values both below as well as above the Coulomb barrier. The same values of ΔR are used to fit the existing fusion excitation data for compound nucleus ^{106}Sn* at similar $E_{\text{c.m.}}/V_b$ values. Also, fusion cross sections are predicted for two energies in the sub-barrier region for the ^{106}Sn* compound nucleus where the experimental fusion cross section is not available. This section describes the significant role of the various parameters incorporated in the model to obtain the cross sections and their importance in addressing the involved decay mechanism of the CN.

To understand the possible effects of the structure of the decaying CNs ^{106}Sn* and ^{106}Cd* formed in the ^{48}Ti + ^{58}Ni and ^{48}Ti + ^{58}Fe reactions, P_0 has been calculated for various fragments or clusters formed inside the CN. P_0 of the respective fragments provides the structural information of the compound nucleus. The preformation probabilities are obtained from the calculated fragmentation potentials in the fragmentation process as discussed in the methodology. So, in order to investigate the possible structures of the involved nuclei, the calculated fragmentation potentials have been plotted with respect to fragment mass in the decay of CNs ^{106}Sn* and ^{106}Cd* at similar $E_{\text{c.m.}}/V_b$'s. Figures 1(a) and 1(b) describe the fragmentation for the extreme values of angular momentum values. It is to be noted that, at $\ell = 0\hbar$, the contribution of the LPs or ERs is more prominent than the intermediate mass fragments and symmetric fission fragments, which, otherwise, start appearing at higher-ℓ values. In the plots, it can be noted that there appears some structure variation with decrease in the N/Z ratio. These figures clearly depict that the α structure shows dips in the fragmentation profile of the system with a lower N/Z value i.e., in the case of ^{106}Sn*, Fig. 1(a), whereas with an increase in the N/Z value in the case of more neutron-rich ^{106}Cd*, Fig. 1(b), the α structure vanishes. This observation is consistent with the earlier work where the fragmentation profile of various isotopes of Ba and Xe nuclei were analyzed [19,20].

Now, these potentially minimized clusters provide an estimate of highly preformed fragments or clusters inside the compound nucleus. As mentioned earlier, no nCN has been observed, and the reported fusion cross sections have contributions from ERs only, so, an extensive analysis of this aspect has been explored by figuring out the contribution of each channel of ERs or LPs ($A \leqslant 4$) towards the cross-section values. For this, we have replotted the fragmentation potential plot for fragment mass $1 \leqslant A_2 \leqslant 4$ at different ℓ values as shown in Figs. 2(a) and 2(b). It can be observed that fragment mass number $A_2 = 1$ remains highly minimized at all ℓ values, although some change in the Z distribution is observed at higher angular momenta in the case of compound nucleus ^{106}Sn* [Fig. 2(a)]. Figures 5(a) and 5(b) are plots for the preformation probability P_0 as a function of angular momentum reemphasis the dominance of fragment mass $A_2 = 1$ at all ℓ values in comparison to other LPs i.e., $A_2 = 2$–4 for both CNs under study.

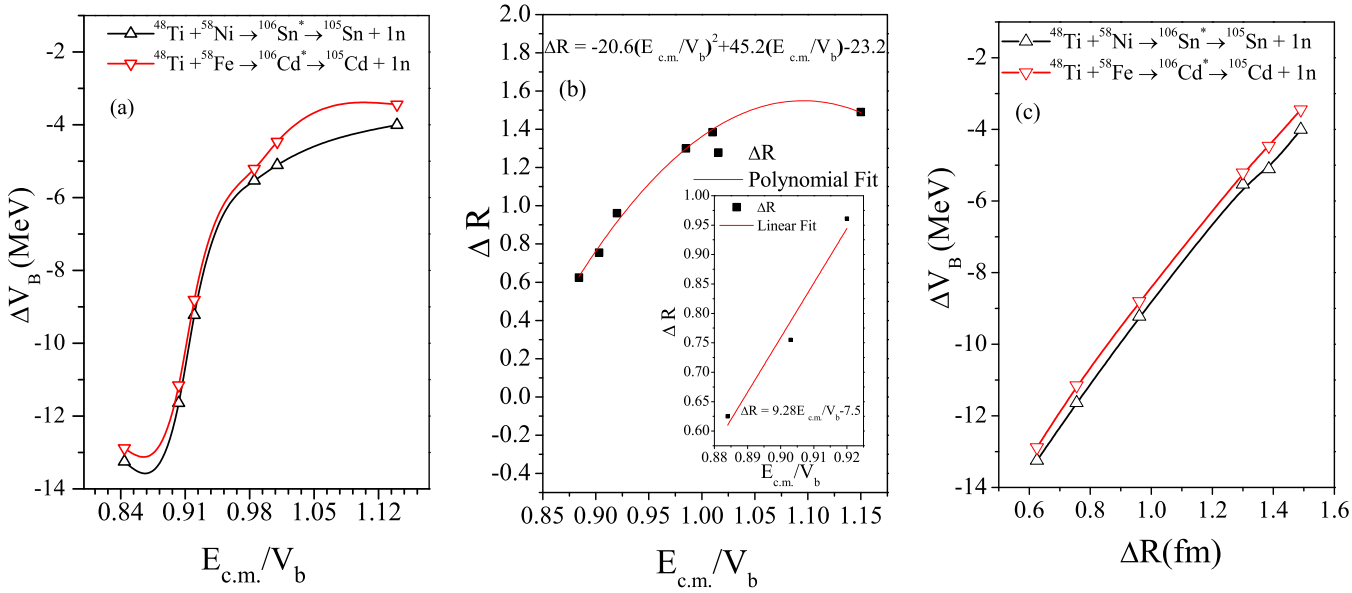

FIG. 4. (a) The variation of the barrier-lowering ΔV_B (at $\ell_{\max}$) as a function of $E_{\mathrm{c.m.}}/V_b$, (b) neck-length parameter ΔR as a function of $E_{\mathrm{c.m.}}/V_b$ obtained for CNs ^{106}Sn* and ^{106}Cd*. The polynomial fit for the equation of ΔR as a function of $E_{\mathrm{c.m.}}/V_b$ is also presented for a whole range of energies, and the linear fit for lowest three energies is also given. (c) Variation of ΔV_B as a function of ΔR.

The tunneling of these energetically favored fragments through the barrier is determined through the scattering potential and penetration probability of these fragments. The scattering potentials for both CNs at the lower ℓ and $\ell_{\max}$ values is shown in Figs. 3(a) and 3(b). The barrier modification (ΔV_B) values, which are the difference between the top of the barrier V_b and the actual potential V_{R_a} used for penetration are also mentioned. It is clear from the plots, presented by Figs. 3(a) and 3(b), that, with an increase in the angular momentum, ΔV_B decreases. Moreover, it is true that as per the statistical model-based coupled-channel calculations (ccc), the phenomenon of fusion hindrance is evident at sub-barrier energies because the coupling effects are too strong. But it is important to note that, in the statistical formalisms, the ER

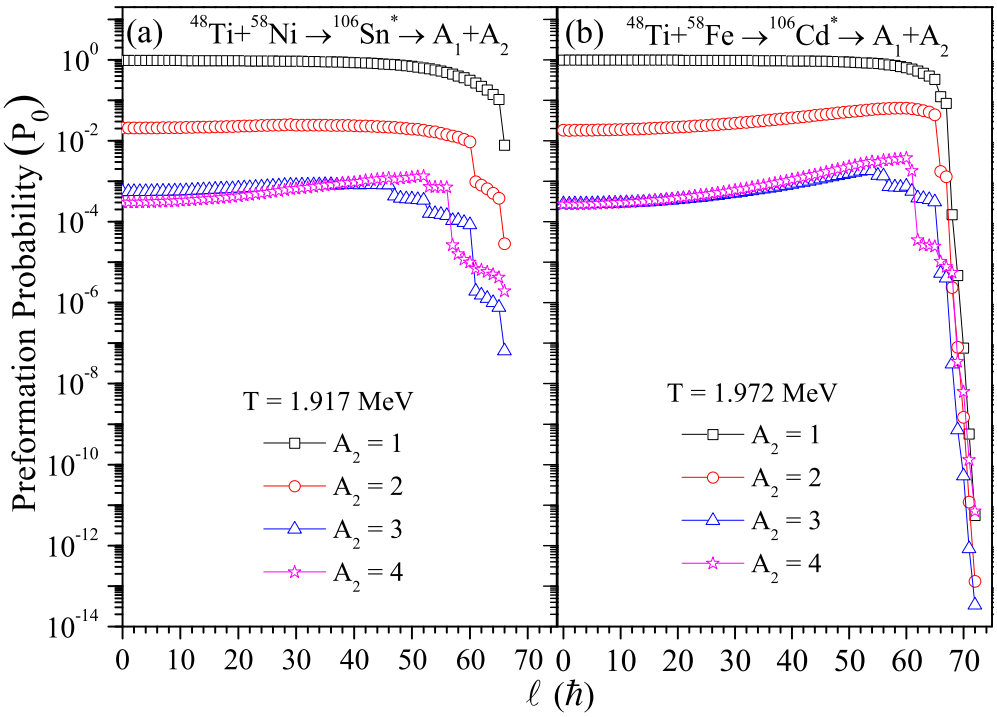

FIG. 5. The preformation probability P_0 as a function of angular momentum for LPs, calculated for the compound systems ^{106}Sn* and ^{106}Cd* at $E_{\mathrm{c.m.}}/V_b = 0.92$ and $\Delta R = 0.96$ fm for deformed fragmentation paths.

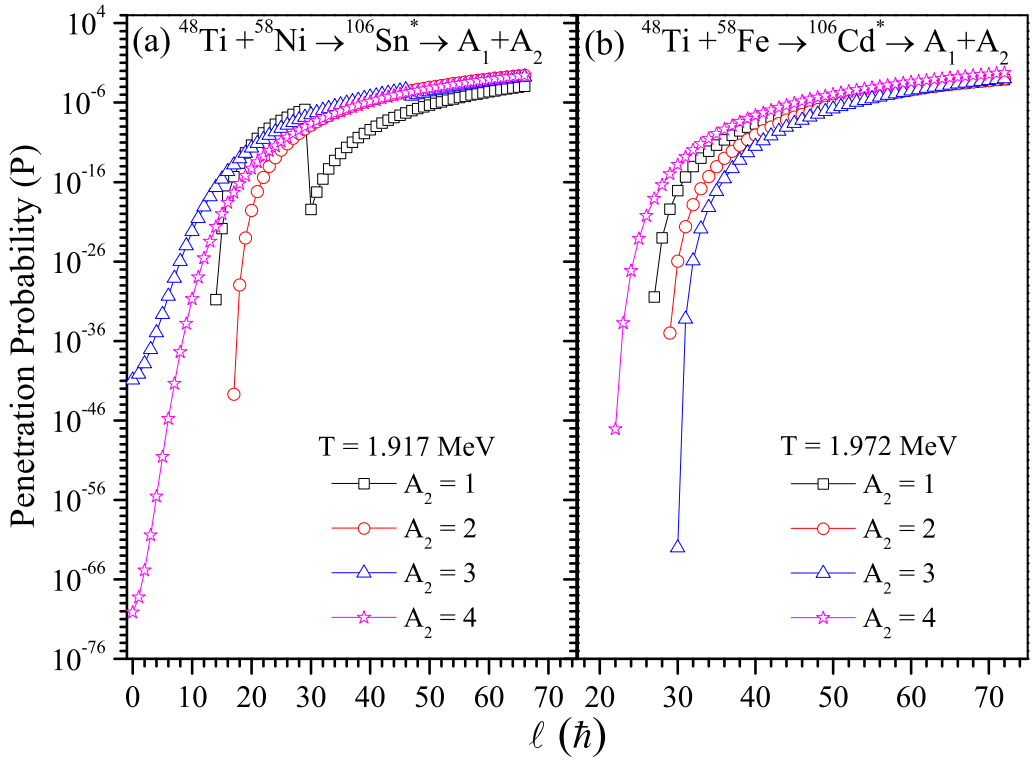

FIG. 6. The variation of penetration probability P as a function of angular momentum ℓ for LPs from compound systems ^{106}Sn* and ^{106}Cd* at $E_{\rm c.m.}/V_b = 0.92$ and $\Delta R = 0.96$ fm for the deformed fragmentation.

and fission are treated differently, whereas the DCM treats all the decay processes on equal footings as barrier penetration of preformed fragments within the collective clusterization approach of quantum-mechanical fragmentation theory. The DCM also supports the only acceptable explanation of hindrance phenomenon in ccc, in terms of barrier-lowering ΔV_B, which is its in-built property. This property is directly related to the variation of ΔR. It may be noted that the need of the barrier-lowering effect in both ER and fission cross sections at sub-barrier energies for a proper interpretation of fusion data for the ^{64}Ni-induced reactions on stable ^{112,118,124}Sn as well as radioactive ^{132}Sn is exercised in the DCM-based work quite explicitly [38].

To study how much barrier modification occurs for a particular compound nucleus, ΔV_B vs the $E_{\rm c.m.}/V_b$ graph is plotted here for energetically favored as well as one of the dominant decay channels, i.e., ^{106}Cd$^{*} \rightarrow ^{105}$ Cd + $1n$ and ^{106}Sn$^{*} \rightarrow ^{105}$ Sn + $1n$ at the highest value of angular momenta as shown in Fig. 4(a). It is observed that the lowering of the barrier increases with a decrease in $E_{\rm c.m.}/V_b$ for both compound systems, which signifies the lower cross sections at lower-energy values. It also indicates that the lowering of barrier values (ΔV_B) required in the case of ^{106}Cd* is lesser in comparison to ^{106}Sn* (having proton shell closure) at all values of $E_{\rm c.m.}/V_b$. Thus, the quantum tunneling of the fragments in the case of compound nucleus ^{106}Cd* through the barrier is less hindered as compared to rigid compound nucleus ^{106}Sn*. Thus, less hindrance threshold is observed at lower-energy values in ^{106}Cd* in comparison to ^{106}Sn*. The dynamics of the neck region are quite different when the two nuclei approach and rebound from each other. Here, in the present paper, the variation of the neck-length parameter for the rebound state is sensitive to the compound nucleus mass and its excitation energy, inclusion of shape parameters, etc. Henceforth, in Fig. 4(b), we have shown the variation of ΔR as a function of $E_{\rm c.m.}/V_b$. A decent polynomial fit has been observed over a range of available energies which, in turn, enable us to predict the below barrier contributions which are not measured so far in the case of ^{106}Sn*. The inset shows the linear fit for lowest below barrier energies also. Recently, across barrier fission analysis of At^{*} isotopes formed in ^{3,4,6,8}He + ^{209} Bi reactions have been made [39] in which the DCM calculations are extended at the below-barrier region for these nuclei. Figure 4(c) shows that, with the increase in ΔR, the barrier-lowering parameter ΔV_B decreases. In other words, at the above barrier energies where barrier modification should be zero, we get a small (∼3-MeV) constant value and the modification is large (∼8–14 MeV) for below-barrier energies.

Now, in calculating the cross section, the penetrability (P) of different fragments through the barrier also plays a significant role. Penetrability profiles for the compound nuclei under study as a function of angular momentum are shown in Figs. 6(a) and 6(b). From the above discussion, we have observed that, as the angular momentum increases, there is a decrease in magnitude of the ΔV_B values, thus, the penetration of fragments as depicted in the plot also increases with the angular momentum of the compound nucleus, which,

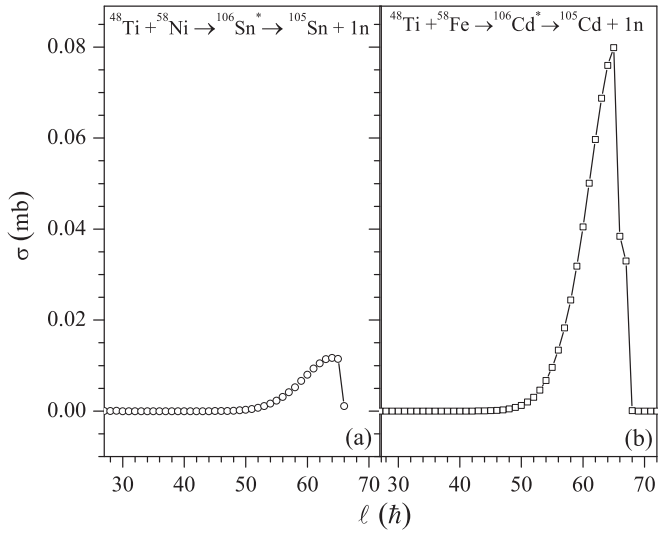

FIG. 7. The cross section of the $1n$ channel as a function of angular momentum ℓ for CNs ^{106}Sn* and ^{106}Cd* at $E_{\text{c.m.}}/V_b = 0.92$ and $\Delta R = 0.96$ fm.

in turn, effects the final cross sections. Furthermore, to see the comparative contribution of the $1n$ channel towards the total cross section for both CNs, variation of the $1n$-channel cross section as a function of ℓ values has been plotted as shown in Fig. 7 for CNs ^{106}Sn* [Fig. 7(a)] and ^{106}Cd* [Fig. 7(b)], respectively. It is quite evident that the fragment mass $A_2 = 1$ contribution is quite large from compound nucleus ^{106}Cd*. Figures 8(a) and 8(b) depicts the ℓ-summed preformation and penetration probability for each fragment, further used to obtain their total contribution towards ℓ-summed fusion cross sections. It can be observed from the plot that the cross sections follow the behavior of ΣP_0, that is, the highly preformed fragment is contributing maximum towards the cross section thereby indicating that the necessary nuclear structure

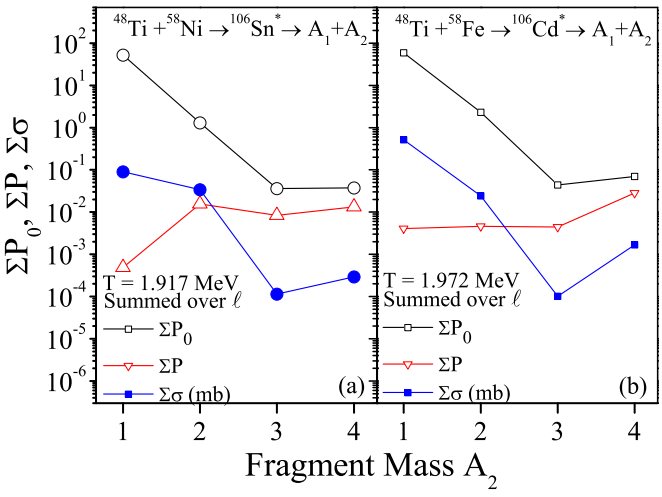

FIG. 8. The comparison of the ℓ-summed preformation probability, penetrability, and cross-section values as a function of fragment mass, i.e., LPs ($A_2 = 1$–4) for CNs ^{106}Sn* and ^{106}Cd* at $E_{\text{c.m.}}/V_b = 0.92$ and $\Delta R = 0.96$ fm.

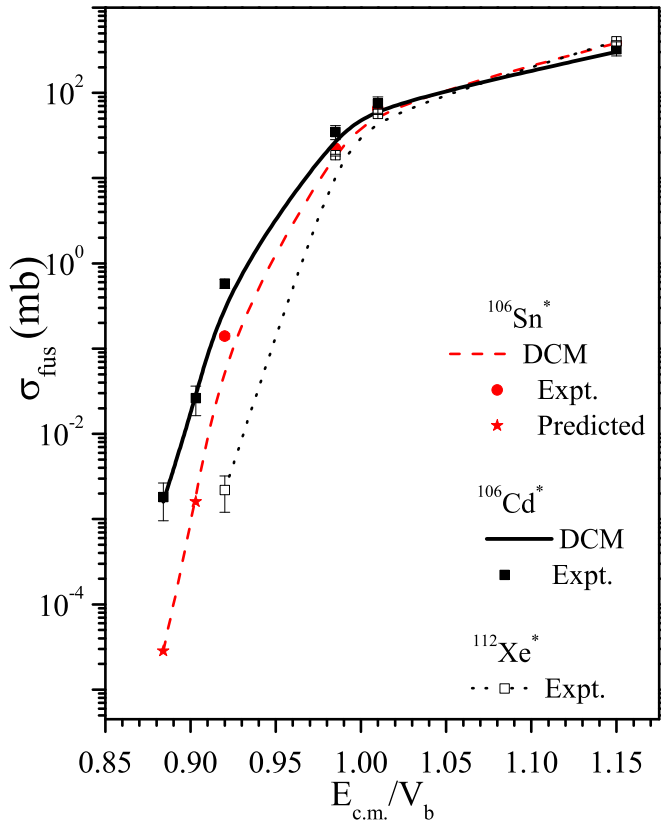

FIG. 9. The fusion cross sections σ_{fus} as a function of $E_{\text{c.m.}}/V_b$ for the decay of two nuclear systems formed in ^{48}Ti-induced reactions for the case of hot compact configurations. Experimental values of σ_{fus} for compound nucleus ^{112}Xe* are also compared [40].

information is contained in P_0 and not in P. Similar behavior is obtained at other energies as well. It is observed that the ΣP_0 value is more for compound nucleus ^{106}Cd* in comparison to ^{106}Sn* at lower values of $E_{\text{c.m.}}/V_b$, particularly, for the $1n$ channel. Thus, the contribution of ΣP_0 is comparatively small towards fusion cross sections at lower values of $E_{\text{c.m.}}/V_b$ in the case of compound nucleus ^{106}Sn*.

The calculated fusion excitation values are plotted as a function of $E_{\text{c.m.}}/V_b$ in Fig. 9. It is observed from the figure that the calculated fusion excitation values are in agreement with the available experimental data. Also, it can be seen that the sub-barrier cross sections of $^{48}\text{Ti} + ^{58}\text{Fe}$ are much larger than those of $^{48}\text{Ti} + ^{58}\text{Ni}$. It can be clearly noted that the cross sections of ^{106}Sn* (dashed line) decrease very steeply at the lowest energies in comparison to ^{106}Cd* (solid line). These observations can be established through the enhanced values of ΣP_0 and lower ΔV_B values of LPs from compound nucleus ^{106}Cd* in comparison to that of compound nucleus ^{106}Sn*. In Fig. 9, experimental fusion cross sections are also plotted for compound nucleus ^{112}Xe* represented by (dotted line + open square) [40]. It can be seen that the fusion cross-section values, which are very less and lie beneath the other two CNs under study, may be due to the fact that they are formed through the rigid structure of projectile and target, respectively, ^{58}Ni and ^{54}Fe having shell closed protons and neutrons.

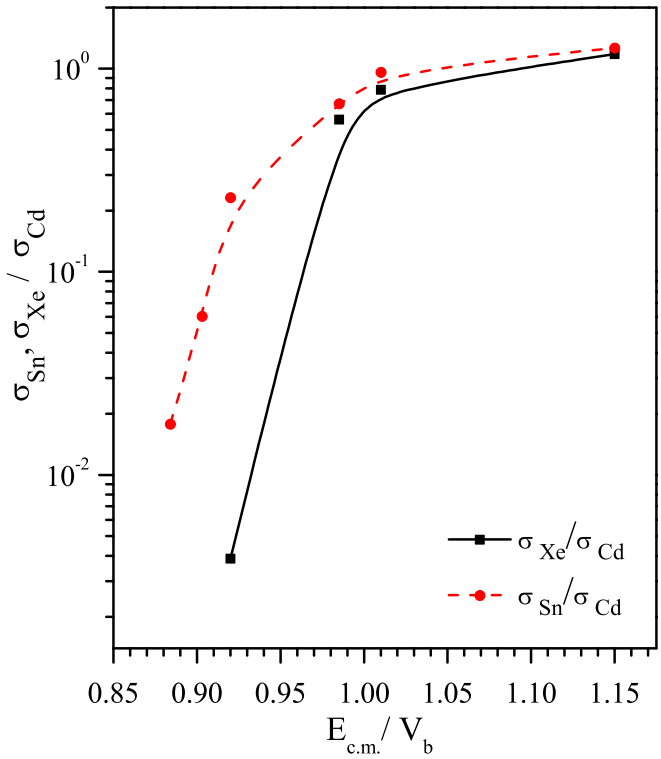

FIG. 10. The ratio of fusion cross sections of ^{106}Sn* and ^{112}Xe* with respect to ^{106}Cd* as a function of $E_{c.m.}/V_b$.

The DCM calculated ER cross sections or σ_{fus} at similar $E_{c.m.}/V_b$ values for β_2-deformed configurations are given in Table I, which are in agreement with the experimental data at all the reported energies. The predicted cross-section values at the lowest two points in the case of compound nucleus ^{106}Sn* are also given in the table. The ℓ_{max} and ΔR values for both systems are also mentioned. The fixed values of ΔR are the same for similar values of $E_{c.m.}/V_b$. This result is consistent with our earlier result where the same values of ΔR were used to reproduce and predict the experimental cross sections at similar $E_{c.m.}/V_b$ values [26]. It is relevant to mention here that it is clear from the calculations that the chosen values of ΔR are reproducing the cross sections of the fully equilibrated ^{106}Cd* compound nucleus at below-barrier energies very well, and we observed no noncompound contribution which implies that the calculated P_{CN} for ^{106}Cd* is 1 as $\sigma_{nCN} = 0$ (which is the difference between calculated and experimental cross-section values), and the same is shown in Table II. This validates the use of the model for such systems and energy ranges. As the masses of the compound nuclei are the same, so is the projectile and the target, and the $E_{c.m.}/V_b$ is similar, so by considering these conditions, we anticipate that the overlapping of similar radii may result in the formation of the ^{106}Sn* compound nucleus as well. Also, using chosen values of ΔR fitted for ^{106}Cd*, no noncompound contribution is observed for ^{106}Sn* as well. So, using this argument, we could write that we can get the idea about the cross sections of ^{106}Sn*, and cross sections can be predicted. And, thus, in the case of ^{106}Sn* P_{CN} will also follow the similar values of P_{CN}. And, it is noted that, for both systems under study, no nCN component is observed and, hence, P_{CN} is taken as 1.

From the above observations, it is clear that the cross sections of compound nucleus ^{106}Sn* (also having $Z = 50$ shell closure) populated in the reaction, which involves only target ^{58}Ni with proton shell closure, are lower than the cross sections of compound nucleus ^{106}Cd*, which is populated through the reaction which has no shell closure for both the projectile as well as the target (^{48}Ti + ^{58}Fe), it will be interesting to further investigate the effect of shell closure on fusion cross sections for the reaction which involves a rigid structure for both the projectile as well as the target. For this, we have chosen the ^{48}Ni + ^{54}Fe reaction populating compound nucleus ^{112}Xe*. The dynamical study of ^{112}Xe* has been performed earlier within the DCM [20]. As mentioned above also, the compound nucleus ^{112}Xe* is formed through the rigid structure of projectile and target. To compare the effect of shell closure on cross sections, the suppression factor has been plotted for ^{106}Sn* and ^{112}Xe* with respect to ^{106}Cd* at similar values of $E_{c.m.}/V_b$ and is shown in Fig. 10. It can

TABLE I. The DCM-calculated fusion cross section σ_{fus} considering the deformed fragmentation path and compared with experimental data [27] for CNs ^{106}Sn* and ^{106}Cd* at similar $E_{c.m.}/V_b$ values.

Reaction	E_{lab} (MeV)	$E_{c.m.}$ (MeV)	$E_{c.m.}/V_b$	T (MeV)	$\ell_{max}(\hbar)$	ΔR (fm)	σ_{fus} (mb) DCM	Expt.
^{48}Ti + ^{58}Ni → ^{106}Sn*	127.82	69.94	0.884	1.885	65	0.625	0.0000335	
	130.57	71.45	0.903	1.890	66	0.755	0.0016	
	132.9	72.73	0.92	1.9172	66	0.961	0.135	0.14 ± 0.01
	142.5	78.0	0.985	2.033	69	1.3	22.23	22.5 ± 1.0
	146.75	80.3	1.01	2.084	69	1.385	69.3	65.6 ± 2.95
	165.8	90.74	1.15	2.287	70	1.49	383.0	384.0 ± 19.0
^{48}Ti + ^{58}Fe → ^{106}Cd*	118.06	64.6	0.884	1.91	68	0.625	0.0018	0.00181 ± 0.000849
	120.62	66.0	0.903	1.94	70	0.755	0.0265	0.0263 ± 0.01
	123.36	67.5	0.92	1.972	72	0.961	0.58	0.58 ± 0.0711
	131.5	72.0	0.985	2.07	74	1.3	33.1	34.8 ± 6.58
	134.87	73.8	1.01	2.11	74	1.385	72.0	75.4 ± 14.3
	152.0	83.2	1.15	2.293	80	1.49	302.2	325.0 ± 54.2

TABLE II. The DCM-calculated fusion cross-section $\sigma_{\rm fus}$ considering the deformed fragmentation path and compared with experimental data for compound nucleus ^{106}Cd*, also $P_{\rm CN}$ and $\sigma_{\rm nCN}$ are mentioned at lower $E_{\rm c.m.}/V_b$ values.

Reaction	$E_{\rm c.m.}/V_b$	ΔR (fm)	$\sigma_{\rm fus}$ (mb) DCM	Expt.	$P_{\rm CN}$	$\sigma_{\rm nCN}$
^{48}Ti + ^{58}Fe → ^{106}Cd*	0.884	0.625	0.0018	0.00181 ± 0.000849	1	0
	0.903	0.755	0.0265	0.0263 ± 0.01	1	0
	0.92	0.961	0.58	0.58 ± 0.0711	1	0

be seen that the suppression factor is almost similar at higher $E_{\rm c.m.}/V_b$ where the ratio for compound nucleus ^{112}Xe* is highly suppressed in comparison to that of compound nucleus ^{106}Sn* at lower values of $E_{\rm c.m.}/V_b$. An onset of the hindrance at energy closer to the Coulomb barrier is quite evident here.

IV. SUMMARY

In the present paper, dynamical aspects along with the role of magicity and the hindrance effects are investigated for CNs ^{106}Sn* and ^{106}Cd*, having the same mass number, formed in the reactions ^{48}Ti + ^{58}Ni and ^{48}Ti + ^{58}Fe at energies around the Coulomb barrier. The available experimental data for these CN have been reproduced within the collective clusterization approach of the DCM to fix the values of neck-length parameter ΔR, the only variable parameter of the DCM, at similar $E_{\rm c.m.}/V_b$ values. It is important to point out here that these values of ΔR are fixed here for one of the reactions ^{48}Ti + ^{58}Fe forming compound nucleus ^{106}Cd* and are used to calculate as well as predict the fusion cross-sections $\sigma_{\rm fus}$ for another reaction ^{48}Ti + ^{58}Ni for the energy values where experimental data are not available. The DCM calculated results are very well compared with the available experiential data. The experimental verification of the results, for which the experiential data are not available, is called for. We find that, for the systems having similar entrance channel asymmetry and the $E_{\rm c.m.}/V_b$ values, ΔR has a uniquely fixed value.

It is noted that the $\sigma_{\rm fus}$ of ^{48}Ti + ^{58}Ni decrease very steeply at the lowest energies in comparison to ^{48}Ti + ^{58}Fe. These observations can be established through the enhanced values of ΣP_0 for LPs, particularly, the $A_2 = 1$ channel from the compound nucleus ^{106}Cd* in comparison to compound nucleus ^{106}Sn*. Moreover, the hindrance factor or barrier modification, i.e., ΔV_B values are lower in the case of LPs' decay of compound nucleus ^{106}Cd* in comparison to that of compound nucleus ^{106}Sn*. It is observed that the ΔV_B increases with a decrease in $E_{\rm c.m.}/V_b$ for both compound systems which implies the lower cross sections at lower-energy values.

Furthermore, it is conjectured that the fusion hindrance at below-barrier energies is maximum for compound nucleus ^{112}Xe* formed through projectile and target (^{58}Ni + ^{54}Fe) having closed-shell structures in the entrance channel and least for the compound nucleus ^{106}Cd* formed with open-shell colliding nuclei (^{48}Ti + ^{58}Fe). The hindrance observed for compound nucleus ^{106}Sn* involving one closed shell colliding nuclei (^{48}Ti + ^{58}Ni) lies in between. Thus, the structure of involved nuclei seems to play an important role in the sub-barrier fusion reaction dynamics, i.e., below the Coulomb barrier.

ACKNOWLEDGMENTS

One of us (R.K.) acknowledges financial assistance from the Inter University Accelerator Centre, New Delhi under Grant No. UFR-59306 and is thankful to the Theoretical Nuclear Physics Research Group, Department of Physics, Sri Guru Granth Sahib World University, Fatehgarh Sahib for support.

[1] B. B. Back, H. Esbensen, C. L. Jiang, and K. E. Rehm, Rev. Mod. Phys. **86**, 317 (2014).
[2] C. L. Jiang *et al.*, Phys. Rev. Lett. **93**, 012701 (2004).
[3] A. M. Stefanini *et al.*, Phys. Rev. C **82**, 014614 (2010).
[4] A. M. Stefanini *et al.*, Phys. Rev. C **92**, 064607 (2015).
[5] S. Misicu and H. Esbensen, Phys. Rev. Lett. **96**, 112701 (2006); Phys. Rev. C **75**, 034606 (2007).
[6] C. H. Dasso and G. Pollarolo, Phys. Rev. C **68**, 054604 (2003).
[7] T. Ichikawa, K. Hagino, and A. Iwamoto, Phys. Rev. Lett. **103**, 202701 (2009); T. Ichikawa, Phys. Rev. C **92**, 064604 (2015).
[8] G. Montagnoli *et al.*, Phys. Rev. C **90**, 044608 (2014); **85**, 024607 (2012); C. L. Jiang *et al.*, *ibid.* **78**, 017601 (2008); A. M. Stefanini *et al.* *ibid.* **78**, 044607 (2008); Phys. Lett. B **679**, 95 (2009).
[9] R. K. Gupta, M. Balasubramaniam, R. Kumar, D. Singh, C. Beck, and W. Greiner, Phys. Rev. C **71**, 014601 (2005).
[10] B. B. Singh, M. K. Sharama, R. K. Gupta, and W. Greiner, Int. J. Mod. Phys. E **15**, 699 (2006).
[11] R. K. Gupta, M. Balasubramaniam, R. Kumar, D. Singh, C. Beck, and W. Greiner, J. Phys. G: Nucl. Part. Phys. **32**, 345 (2006).
[12] B. B. Singh, M. K. Sharma, and R. K. Gupta, Phys. Rev. C **77**, 054613 (2008).
[13] R. Kumar, M. Bansal, S. K. Arun, and R. K. Gupta, Phys. Rev. C **80**, 034618 (2009).
[14] S. Kanwar *et al.*, Int. J. Mod. Phys. E **18**, 1453 (2009).
[15] S. K. Arun, R. Kumar, and R. K. Gupta, J. Phys. G: Nucl. Part. Phys. **36**, 085105 (2009).

[16] R. K. Gupta, S. K. Arun, R. Kumar, and M. Bansal, Nucl. Phys. **A834**, 176c (2010).
[17] M. K. Sharma, S. Kanwar, G. Sawhney, and R. K. Gupta, Phys. Rev. C **85**, 064602 (2012).
[18] B. B. Singh *et al.*, Proc. DAE Symp. Nuc. Phys. **56**, 474 (2011); **57**, 550 (2012); http://www.sympnp.org/proceedings/; EPJ Web Conf. **86**, 00048 (2015); B. B. Singh *et al.*, Phys. Rev. C **95**, 014611 (2017); **99**, 014614 (2019).
[19] M. Kaur, R. Kumar, and M. K. Sharma, Phys. Rev. C **85**, 014609 (2012).
[20] M. Kaur and M. K. Sharma, Eur. Phys. J. A **50**, 61 (2014).
[21] K. Sandhu, M. K. Sharma, and R. K. Gupta, Phys. Rev. C **85**, 024604 (2012); **86**, 064611 (2012).
[22] M. Bansal, S. Chopra, R. K. Gupta, R. Kumar, and M. K. Sharma, Phys. Rev. C **86**, 034604 (2012).
[23] G. Kaur and M. K. Sharma, Nuc. Phys. A **884**, 36 (2012); Phys. Rev. C **87**, 044601 (2013).
[24] Niyti and R. K. Gupta, Phys. Rev. C **89**, 014603 (2014).
[25] M. Kaur *et al.*, Phys. Rev. C **92**, 024623 (2015); Proc. DAE Symp. Nucl. Phys. **61**, 592 (2016); **62**, 520 (2017); http://www.sympnp.org/proceedings/; Int J. Pure Appl. Phys **13**, 154 (2017); Nuc. Phys. A **980**, 67 (2018).
[26] R. Kaur, M. Kaur, V. Singh, S. Kaur, B. B. Singh, and B. S. Sandhu, Phys. Rev. C **98**, 064612 (2018).
[27] A. M. Vinodkumar, K. M. Varier, N. V. S. V. Prasad, D. L. Sastry, A. K. Sinha, N. Madhavan, P. Sugathan, D. O. Kataria, and J. J. Das, Phys. Rev. C **53**, 803 (1996).
[28] A. Bonasera *et al.*, Phys. Lett. **141B**, 9 (1984); Nuc. Phys. **A439**, 353 (1985); Phys. Rev. C **34**, 740 (1986).
[29] H. Kröger and W. Scheid, J. Phys. G: Nucl. Part. Phys. **6**, L85 (1980).
[30] R. K. Gupta *et al.*, Phys. Rev. Lett. **35**, 353 (1975); A. Săndulescu, R. K. Gupta *et al.*, Phys. Lett. B **60**, 225 (1976); R. K. Gupta *et al.*, *ibid.* **67**, 257 (1977).
[31] G. Royer and M. Mignen., J. Phys. G: Nucl. Part. Phys. **18**, 1781 (1992).
[32] N. J. Davidson, S. S. Hsiao, J. Markram, H. G. Miller, and Y. Tzeng, Nucl. Phys. **A570**, 61c (1994).
[33] W. Myers and W. J. Swiatecki, Nucl. Phys. **81**, 1 (1966).
[34] A. S. Jensen and J. Damgaard, Nucl. Phys. **A203**, 578 (1973).
[35] J. Blocki, J. Randrup, W. J. Swiatecki, and C. F. Tsang, Ann. Phys. (NY) **105**, 427 (1977).
[36] P. Moller, J. R. Nix, W. D. Myers, and W. J. Swiatecki, At. Data Nucl. Data Tables **59**, 185 (1995).
[37] S. S. Malik and R. K. Gupta, Phys. Rev. C **39**, 1992 (1989).
[38] M. K. Sharma *et al.*, J. Phys. G: Nucl. Part. Phys. **38**, 055104 (2011).
[39] A. Kaur *et al.*, Nucl. Phys. **A940**, 94 (2019).
[40] A. M. Stefanini *et al.*, Phys. Rev. C **81**, 037601 (2010).